Evaluation of a metal artifact reduction algorithm and an optimization filter in the estimation of peri-implant dehiscence defects by using cone beam computed tomography: an in-vitro study

Seval Bayrak, DDS, PhD,[a] Kaan Orhan,[b,c] Emine Sebnem Kursun Çakmak,[d] Cansu Görürgöz,[e] Onur Odabaşı,[f] Dervis Yilmaz,[g] and Cemal Atakan[h]

Objectives. The aim of this study was to assess the effect of a metal artifact reduction (MAR) algorithm and the adaptive image noise optimizer (AINO) optimization filter in the detection of peri-implant dehiscences with cone beam computed tomography (CBCT).

Study Design. Nine implants (3 zirconium, 3 titanium, and 3 zirconium-titanium) were placed in 3 sheep heads. Dehiscences were created on the buccal and lingual/palatal surfaces. A total of 9 defects and 9 controls with no defects were evaluated by 3 observers. Each sheep head was scanned 5 times with 4 scan modes; (1) without MAR/without AINO; (2) with MAR/without AINO; (3) without MAR/with AINO; and (4) with MAR/with AINO. Receiver operating characteristic analysis and weighted kappa coefficients were used to calculate diagnostic efficacy and intra- and interobserver agreements for each implant type and scan mode.

Results. For all implant types, dehiscences were most accurately detected when both MAR and AINO were applied ($P \leq .045$). Detection of dehiscences was more accurate with titanium implants ($P \leq .040$). There were no significant differences in agreement among and between the observers.

Conclusions. The use of both MAR and AINO enhanced the detection accuracy of artificially created dehiscences in proximity to implants. Their combined use is recommended for detecting peri-implant dehiscences. (Oral Surg Oral Med Oral Pathol Oral Radiol 2020;130:209−216)

Absence of cortical bone in the cervical portion of the alveolar process around an implant is called *peri-implant dehiscence*. It may occur as a result of unfavorable anatomic conditions, including insufficient bone and gingival thickness, incorrect implant placement during surgery, inflammation-generated biofilm, and excessive loading.[1-3] Early diagnosis is important because these defects can cause gingival recession, bone loss, and implant failure.[1,2,4]

[a]Assistant Professor, Department of Dentomaxillofacial Radiology, Faculty of Dentistry, Bolu Abant İzzet Baysal University, Ankara, Turkey.
[b]Professor, Department of Dentomaxillofacial Radiology, Faculty of Dentistry, Ankara University, Ankara, Turkey.
[c]Professor, OMFS IMPATH Research Group, Department of Imaging & Pathology, Faculty of Medicine, University of Leuven and Oral & Maxillofacial Surgery, University Hospitals Leuven, Leuven, Belgium.
[d]Associate Professor, Turkiye Public Hospitals Agency, Ministry of Health, Ankara, Turkey.
[e]Assistant Professor, Department of Dentomaxillofacial Radiology, Faculty of Dentistry, Bursa Uludag University, Bursa, Turkey.
[f]Assistant Professor, Department of Dentomaxillofacial Surgery, Faculty of Dentistry, Yıldırım Beyazıt University, Ankara, Turkey.
[g]Professor, Department of Dentomaxillofacial Surgery, Faculty of Dentistry, Gazi University, Ankara, Turkey.
[h]Professor, Department of Statistics, Faculty of Sciences, Ankara University, Ankara, Turkey.
Received for publication Jan 30, 2020; accepted for publication Feb 7, 2020.

2212-4403/$-see front matter
https://doi.org/10.1016/j.oooo.2020.02.005

Radiographs are required to detect covered anatomic structures, such as the alveolar bone. They expose the degree of interdental and interradicular bone loss, root length, crown−root ratio, periodontal ligament space, and any pathoses around the tooth.[5] Intraoral radiographs are commonly used to evaluate the site after implant placement. However, they may not provide sufficient information to diagnose peri-implant dehiscence defects if there are subtle changes in the initial phase and if they occur on the buccal and lingual sides of the implant because of the 2-dimensional nature of the radiograph and superposition of surrounding anatomic structures.[6] Cone beam computed tomography (CBCT) is currently considered the superior method[7] for providing accurate and reliable information with high-resolution images and low radiation doses (compared with multidetector computed tomography [CT]) in axial, sagittal, coronal, and cross-sectional planes.[8]

The main limitations of CBCT are beam hardening and streaking artifacts, which are caused by high-density materials such as metal and amalgam restorations, root filling materials, and zirconium and titanium implants. These artifacts include dark bands and linear

Statement of Clinical Relevance

A metal artefact reduction algorithm and an optimization filter can be useful in the detection of peri-implant dehiscence defects, and they should be developed by CBCT manufacturers.

streaks around materials that adversely affect the quality of images and may result in misdiagnosis.[7]

CBCT manufacturers have developed different methods to reduce the adverse effects of these artifacts to improve image quality. One method involves changing the exposure parameters (e.g., field of view [FOV], voxel size, peak kilovoltage [kVp], milliamperage [mA], and exposure time).[9] In addition, metal artifact reduction (MAR) algorithms, which improve image quality by performing mathematical algorithms on the raw data after the scanning process during reconstruction, have been developed. This software, however, may also prevent clinicians from seeing the details of the main region of interest while removing streaking around the material by eliminating the effects of beam hardening and streaking artifacts. Additional disadvantages of this software are the extension of reconstruction times and the requirement for massive computer power.[10,11]

A new imaging setting, adaptive image noise optimizer (AINO), has recently become available with the Planmeca ProMax 3-dimensional (3-D) CBCT units (Planmeca Oy, Helsinki, Finland). AINO analyzes exposure data and differentiates noise from fine details during reconstruction, thereby improving image quality by reducing noise. Noise is inherent in scans that use extremely small voxel sizes, and this optimization filter (OF) can be used to mitigate the increase in noise seen with small voxels.[12]

The aim of this study was to assess the effects of MAR and AINO on the detection accuracy of artificially created dehiscences in proximity to different implants in sheep jaws. The null hypothesis stated that there is no significant difference in the detection of these defects on radiographs with or without the use of MAR and AINO.

MATERIALS AND METHODS

Sample preparation

On the basis of a previous study,[13] a power calculation was performed, and sample size was determined (G*Power 3.1 software; Heinrich Heine University, Dusseldorf, Germany). This study was carried out using 3 sheep heads including soft tissues and 3 types of dental implants: zirconium (n = 3); titanium (n = 3); and zirconium-titanium (n = 3). One oral surgeon with 7 years of experience placed all of the implants in the sheep jaws (Figure 1). The implants were inserted with a subcrestal incision to reflect the mucoperiosteal flap. The osteotomy was initiated by using a pilot drill, followed by sequential drilling to prepare the site according to the selected implant size. Copious irrigation with saline was done during the surgical procedure. Each implant was inserted with the use of an insertion tool and a torque wrench. After implant placement, the same surgeon created standardized artificial dehiscence defects in the alveolar bone around the implants. The mucoperiosteal flap was then closed. Care was taken not to damage the peri-implant gingiva.

Fig. 1. Photograph of the positioned implants in a sheep's jaw.

The simulated defects were created at the cervical portion of the bone around the implant in the buccal or lingual/palatal surfaces. The defects were half-elliptic forms, 3 mm in diameter, prepared with high-speed equipment and use of copious air/water spray and rounded diamond burs (KG Sorensen, Zenith Dental Aps, Agerskov, Denmark). In total, 9 dehiscences (5 buccal, 4 lingual/palatal) were created. Nine surfaces (4 buccal, 5 lingual/palatal) were free of dehiscence and used as the control group. The known status of dehiscence defects at each site served as the gold standard for the CBCT examination.

Radiographic imaging

To provide standardization during CBCT imaging, the sheep heads were fixed to the machine during scanning. All images were obtained by using a Planmeca Promax 3-D Max CBCT unit with 4 scan modes: (1) without MAR/without AINO; (2) with MAR/without AINO; (3) without MAR/with AINO; and (4) with MAR/with AINO. The scanning parameters were 90 kVp, 10 mA, and exposure time of 12 seconds with a 0.100 mm^3 voxel size and a 5 × 5.5 cm FOV. Each scan mode was repeated 5 times for each sheep head, producing a total of 60 CBCT scans. After image acquisition, all evaluations were performed on a 21.3-inch flat panel color active matrix TFT medical display (NEC MultiSync MD215 MG; NEC, München, Germany) with a resolution of 2048 × 2560 at 75 Hz and 0.17-mm dot pitch operated at 11.9 bits. Examples of a titanium implant image, with or without simulated peri-implant dehiscence defects using the 4 scan modes, are shown in Figures 2 and 3, respectively.

Image analysis

Each scan was evaluated by 3 observers with 8 to 12 years of experience in CBCT imaging. All reconstructions were performed by using the unit's software (Romexis 4.6). Before beginning the CBCT evaluations in the study, the observers were trained on the

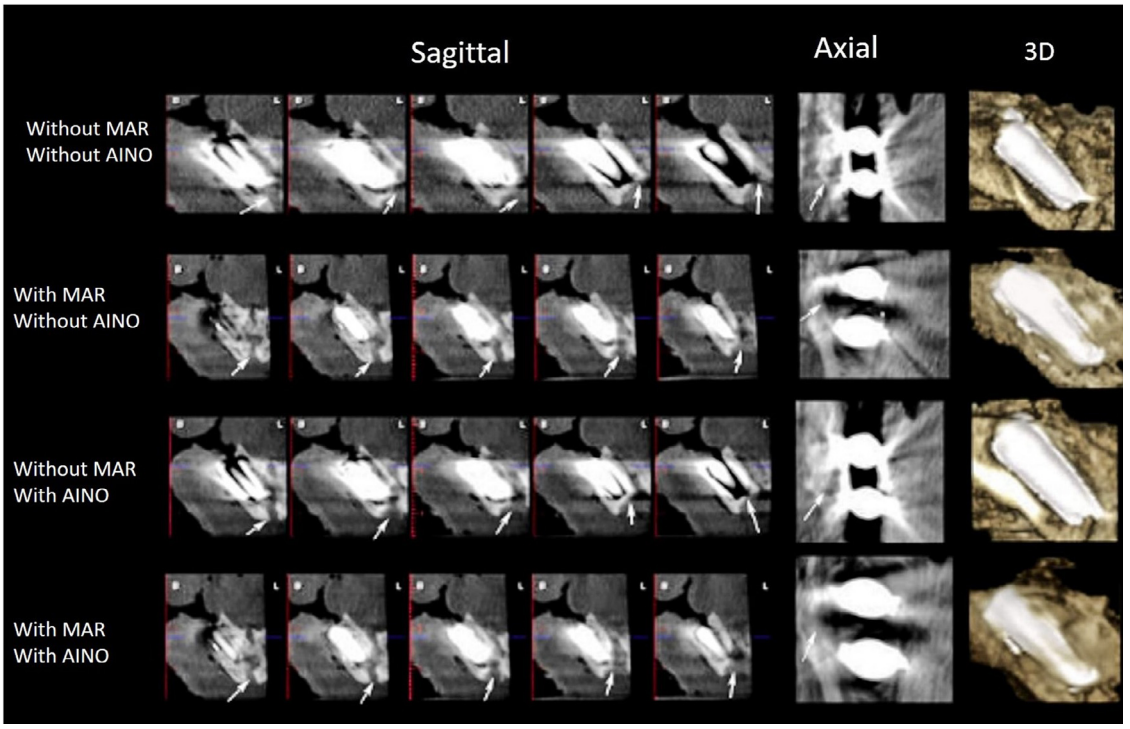

Fig. 2. Sagittal, axial, and 3-dimensional (3-D) slices from cone beam computed tomography (CBCT) images of a titanium implant with simulated peri-implant dehiscence defects *(white arrows)* with 4 scan modes: without metal artifact reduction (MAR)/without the adaptive image noise optimizer (AINO); with MAR/without AINO; without MAR/with AINO; and with MAR/with AINO.

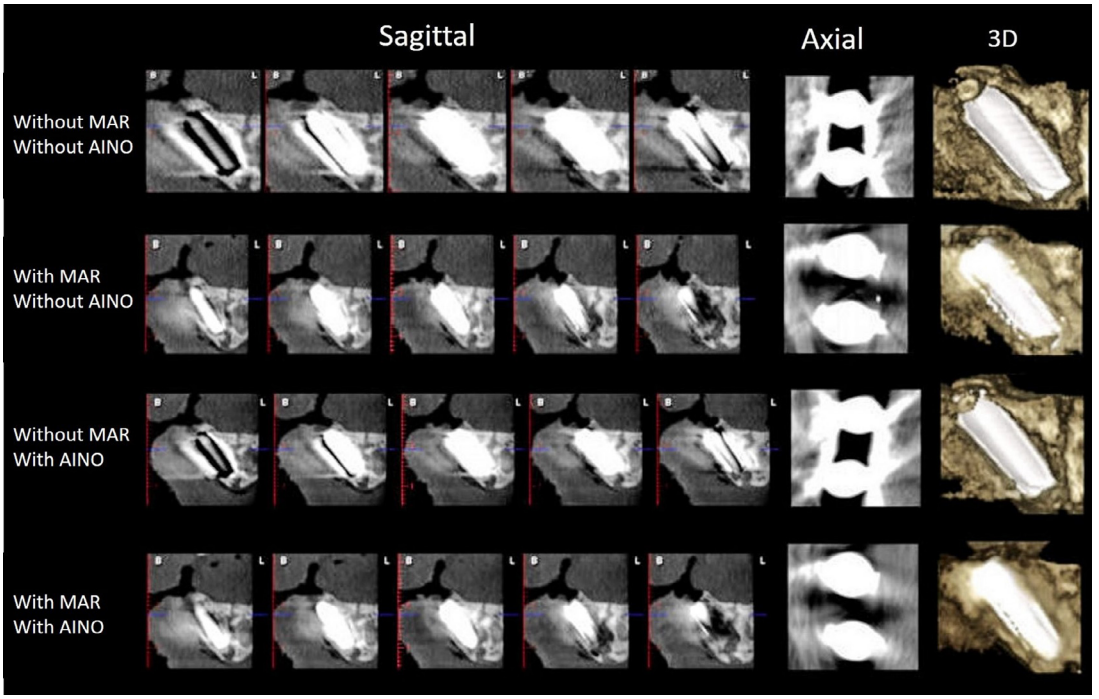

Fig. 3. Sagittal, axial, and 3-dimensional (3-D) slices from cone beam computed tomography (CBCT) images of a titanium implant without simulated peri-implant dehiscence defects with 4 scan modes: without metal artifact reduction (MAR)/without the adaptive image noise optimizer (AINO); with MAR/without AINO; without MAR/with AINO; and with MAR/with AINO.

appropriate use of the software in a special session. Moreover, 5 CBCT images with dehiscences were used to define and calibrate the software for the appearance of dehiscences before the observers began their evaluations. The observers were free to use the software's properties for enhancement and processing functions. The images were anonymized during evaluation of the dehiscences.

The observers were asked to indicate their confidence in the presence or absence of a dehiscence at each site using a 5-point scale: (1) definitely absent; (2) probably absent; (3) unsure; (4) probably present; and (5) definitely present. Each image set was viewed at 1-week intervals, and evaluations of each image set were repeated 2 months after the initial viewing.

Examiner reliability and statistical analysis

Statistical analyses were performed by using SPSS software version 25 (SPSS Inc., Chicago, IL) by calculating and comparing the areas under the receiver operating characteristic (ROC) curves (Az values) for each image set/observer with the significance level set at α= 0.05. This statistical test evaluated the probability of making the correct decision and, therefore, is a measure of diagnostic efficacy related to the use of the different combinations of MAR and AINO. Weighted kappa coefficients were calculated to assess both intra- and interobserver agreements for each image set. Weighted kappa values were interpreted according to the guidelines of Landis and Koch, as adapted by Altman ($\kappa \leq 0.20$, poor; $\kappa = 0.21-0.40$, fair; $\kappa = 0.41-0.60$, moderate; $\kappa = 0.61-0.80$, good; and $\kappa = 0.81-1.00$, very good).[14]

RESULTS

Az values were calculated for each scan mode, implant type, and observer by using both readings (Table I). Az values ranged from 0.580 to 0.750 for scans without MAR and without AINO and ranged from 0.722 to 0.956 for scans with MAR and with AINO; the difference between the values for these scan modes was significant (P = .033). Az values were also significantly higher for scans with MAR/without AINO and without MAR/with AINO compared with the scans without MAR/without AINO (P = .037 and .040, respectively) and significantly lower compared with the scans with MAR and with AINO (P = .040 and .045, respectively). No statistically significant differences were found between the Az values for scans with MAR and without AINO versus scans without MAR and with AINO (P = .182).

Az values ranged from 0.580 to 0.875 for zirconium implants, 0.625 to 0.956 for titanium implants, and 0.580 to 0.813 for zirconium-titanium implants. In summary, titanium implants had significantly higher Az values compared with zirconium and zirconium-

Table I. Az values according to scan modes and implant types for first and second readings of the observers

		Observer 1		*Observer 2*		*Observer 3*	
Scan mode	*Implant type*	*First reading Az–SE*	*Second reading Az–SE*	*First reading Az–SE*	*Second reading Az–SE*	*First reading Az–SE*	*Second reading Az–SE*
1	1	0.580–0.106	0.660–0.102	0.688–0.118	0.580–0.106	0.667–0.122	0.580–0.106
	2	0.691–0.097	0.722–0.106	0.722–0.106	0.750–0.087	0.691–0.097	0.688–0.118
	3	0.580–0.106	0.667–0.122	0.660–0.102	0.722–0.106	0.580–0.106	0.667–0.122
2	1	0.711–0.096	0.722–0.106	0.660–0.102	0.688–0.118	0.711–0.096	0.625–0.102
	2	0.776–0.90	0.738–0.091	0.750–0.087	0.625–0.102	0.776–0.90	0.738–0.091
	3	0.660–0.102	0.625–0.102	0.711–0.096	0.802–0.092	0.711–0.096	0.738–0.091
3	1	0.625–0.102	0.711–0.096	0.750–0.087	0.660–0.102	0.625–0.102	0.660–0.102
	2	0.660–0.102	0.691–0.097	0.800–0.087	0.776–0.90	0.667–0.122	0.711–0.096
	3	0.660–0.102	0.625–0.102	0.722.–0.106	0.711–0.096	0.580–0.106	0.625–0.102
4	1	0.813–0.080	0.875–0.064	0.750–0.087	0.800–0.087	0.802–0.092	0.722–0.106
	2	0.944–0.370	0.956–0.032	0.875–0.064	0.833–0.075	0.944–0.370	0.800–0.087
	3	0.813–0.087	0.811–0.081	0.813–0.080	0.722–0.106	0.811–0.081	0.750–0.087

Scan modes: (1) Without metal artifact reduction (MAR) and without adaptive image noise optimizer (AINO); (2) with MAR and without AINO; (3) without MAR and with AINO; (4) with MAR and with AINO filters following exposure parameters.
Implant types: (1) zirconium implant, (2) titanium implant, (3) zirconium-titanium implant.
SE, standard error.

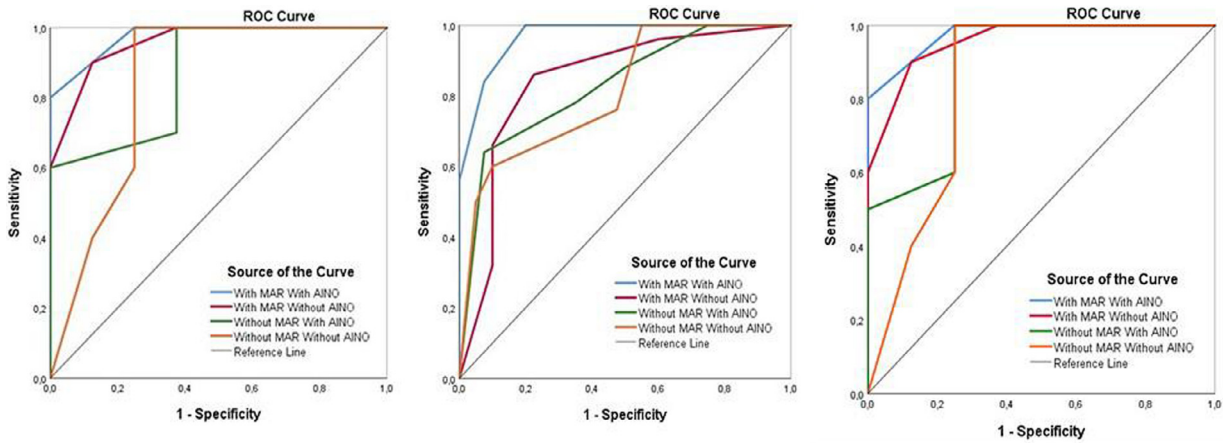

Fig. 4. Receiver operating characteristic (ROC) curves for each scan mode for observer 1 **(A)**, observer 2 **(B)**, and observer 3 **(C)**.

titanium implants ($P = .040$ and $P = .031$, respectively). No significant differences were found between zirconium and zirconium-titanium implants according to Az values ($P = .221$). Figure 4 shows the ROC curves for observers 1, 2, and 3, respectively.

No statistically significant differences were detected among and between observers for any of the scan modes ($P \geq .05$) Weighted kappa coefficients were lowest in the scan mode without MAR/without AINO than in the other 3 modes ($P \leq .05$). This means that this scan mode resulted in the poorest agreement among and between observers on the presence or absence of dehiscences (fair to good agreement) compared with the other 3 scan modes (moderate to very good agreement). Intra- and interobserver weighted kappa coefficients calculated by scan mode are shown in Tables II and III, respectively.

DISCUSSION

An accurate and reliable imaging method and a suitable scanning protocol are essential for clinicians to identify the alveolar bone level and detect defects around the implant. This information is crucial for postoperative assessment of the implant and to select the appropriate treatment procedures, if necessary.[15] Previous studies have evaluated the detection of peri-implant

Table II. Intraobserver weighted kappa coefficients calculated by scan modes and implant types for each observer

	Weighted kappa (SE)		
Zirconium	*Observer 1*	*Observer 2*	*Observer 3*
Without MAR/Without AINO	0.467 (0.128)	0.567 (0.128)	0.378 (0.064)
With MAR/Without AINO	0.667 (0.128)	0.633 (0.072)	0.639 (0.076)
Without MAR/With AINO	0.598 (0.084)	0.633 (0.072)	0.567 (0.128)
With MAR/With AINO	0.717 (0.065)	0.771 (0.158)	0.816 (0.095)
	Weighted kappa (SE)		
Titanium	*Observer 1*	*Observer 2*	*Observer 3*
Without MAR/Without AINO	0.667 (0.073)	0.743 (0.045)	0.667 (0.065)
With MAR/Without AINO	0.778 (0.158)	0.767 (0.056)	0.671 (0.108)
Without MAR/With AINO	0.714 (0.054)	0.800 (0.067)	0.750 (0.084)
With MAR/With AINO	0.856 (0.084)	0.909 (0.101)	0.835 (0.084)
	Weighted kappa (SE)		
Zirconium-Titanium	*Observer1*	*Observer 2*	*Observer 3*
Without MAR/Without AINO	0.350 (0.074)	0.434 (0.048)	0.487 (0.095)
With MAR/Without AINO	0.612 (0.078)	0.548 (0.056)	0.455 (0.054)
Without MAR/With AINO	0.567 (0.079)	0.655 (0.058)	0.498 (0.068)
With MAR/With AINO	0.667 (0.057)	0.729 (0.064)	0.571 (0.076)

AINO, adaptive image noise optimizer; *MAR,* metal artifact reduction; *SE,* standard error.

Table III. Interobserver weighted kappa coefficients value and standard error according to scan modes and implant types for first and second readings

		Observers 1–2		*Observers 1–3*		*Observers 2–3*	
Scan mode	*Implant type*	*First reading κ (SE)*	*Second reading κ (SE)*	*First reading κ (SE)*	*Second reading κ (SE)*	*First reading κ (SE)*	*Second reading κ (SE)*
1	1	0.250 (0.184)	0.471 (0.158)	0.367 (0.128)	0.455 (0.158)	0.571 (0.158)	0.571 (0.158)
	2	0.498 (0.111)	0.663 (0.069)	0.467 (0.128)	0.573 (0.098)	0.550 (0.076)	0.667 (0.128)
	3	0.467 (0.128)	0.534 (0.148)	0.412 (0.099)	0.467 (0.128)	0.667 (0.128)	0.634 (0.148)
2	1	0.571 (0.158)	0.567 (0.128)	0.567 (0.128)	0.667 (0.128)	0.567 (0.128)	0.567 (0.128)
	2	0.624 (0.043)	0.667 (0.128)	0.671 (0.058)	0.700 (0.056)	0.645 (0.056)	0.633 (0.128)
	3	0.500 (0.124)	0.448 (0.056)	0.571 (0.158)	0.571 (0.158)	0.548 (0.156)	0.448 (0.156)
3	1	0.550 (0.124)	0.623 (0.072)	0.560 (0.068)	0.512 (0.124)	0.634 (0.056)	0.500 (0.124)
	2	0.612 (0.067)	0.668 (0.124)	0.671 (0.058)	0.667 (0.128)	0.678 (0.089)	0.600 (0.124)
	3	0.500 (0.124)	0.500 (0.167)	0.512 (0.064)	0.520 (0.084)	0.667 (0.128)	0.455 (0.158)
4	1	0.712 (0.078)	0.571 (0.158)	0.689 (0.084)	0.613 (0.184)	0.634 (0.054)	0.671 (0.058)
	2	0.846 (0.131)	0.812 (0.131)	0.777 (0.184)	0.813 (0.184)	0.690 (0.083)	0.709 (0.131)
	3	0.667 (0.174)	0.740 (0.184)	0.571 (0.158)	0.771 (0.158)	0.571 (0.158)	0.629 (0.078)

Scan modes: (1) without metal artifact reduction (MAR) and without adaptive image noise optimizer (AINO); (2) with MAR and without AINO; (3) without MAR and with AINO; (4) with MAR and with AINO filters following exposure parameters.
Implant types: (1) zirconium implant, (2) titanium implant, (3) zirconium-titanium implant.
SE, standard error.

dehiscence defects by using CBCT,[16] mainly in dry human mandibles.[15] However, in this investigation, we used sheep heads, which have the potential to retain the soft tissue around implants because the soft tissue and the bone itself are in the path of the X-ray beam.

Bony dehiscences and fenestrations cannot be visualized by conventional 2-dimensional radiography because of the superimposition of the cortical bone and/or the dental structures. Thus, CBCT is a better diagnostic tool than conventional radiography for detecting periodontal bone defects.[9] However, most studies do not take into account the exposure parameters, such as kVp, mA, exposure time, voxel size, and FOV.[5] Despite many reports in the literature regarding the effect of voxel size on root fracture, internal and external root resorption, and caries detection,[17-20] there are only a few studies on the impact of voxel size on the visibility of periodontal bone defects.[9,21] Moreover, only very limited information has been published regarding OFs.[12,15]

There are several algorithms that can be applied for CBCT imaging, such as MAR and noise reduction algorithms to help increase image quality during reconstruction. In the ProMax CBCT unit, the MAR algorithm is power based on a selected threshold, and all voxels with higher density are corrected, thus reducing artifacts.[22] Queiroz et al.[23] stated that the Planmeca MAR algorithm is applied after automatic thresholding of raw images in the voxel values corrupted by artifacts, followed by image correction; this suggests that this is a postprocessing algorithm. Planmeca AINO is an OF that purports to remove noise. It allows for lowering exposure values in all imaging modes by reducing noise and helps improve image quality when using small voxel sizes. However, no further information has been published regarding the processing method.

Parrone et al.[12] compared the efficacy of 0.75 mm^3 and 0.100 mm^3 voxel sizes to detect root fractures in endodontically treated teeth and reported no statistically significant difference. However, the 0.75 mm^3 voxel size radiation dose was greater than the dose with the 0.100 mm^3 voxel size (9.2 mGy and 7.4 mGy, respectively). Thus, to make comparisons, the 0.100 mm^3 voxel size was chosen in the present research.

In a recent study, Bechara et al.[24] investigated the effects of MAR modes in contrast-to-noise ratio and concluded that the MAR module increased contrast-to-noise ratio values and that the MAR mode should be used for better images. In another investigation, Bechara et al.[25] compared MAR mode accuracy of root fracture detection in endodontically treated teeth with 2 CBCT units and stated that accuracy was significantly higher without the MAR mode than with the MAR mode.

Kamburoğlu et al.[26] evaluated the diagnostic efficacy of 4 different artifact image modes (without artifact

reduction and with artifact reduction in low, medium, and high modes) for simulated endodontic furcal perforations in endodontically treated teeth and reported that image modes performed similarly for detecting endodontic furcal perforations. Another ex vivo study by Kamburoğlu et al.[15] estimated the accuracy of CBCT images acquired with or without the MAR algorithm in detecting buccal periodontal and peri-implant defects and found no difference among images.

Our results are similar to those of the previously published studies. The performance of the observers for detecting peri-implant dehiscences was similar with or without MAR. However, in this study, an AINO filter was also used, and the observers had significantly better results on scans with both MAR and AINO than on the other 3 combinations of MAR and AINO ($P \leq .045$). Parrone et al.[12] tested AINO to detect root fractures in endodontically treated teeth and found no significant improvement in accuracy with AINO.

Recently, Vasconcelos et al.[27] assessed zirconium implant artifacts with different exposure parameters, both with and without the MAR mode, in a ProMax 3-D CBCT unit and determined that MAR reduced the artifact value. In line with the findings of that study, the MAR algorithm investigated here also was found to reduce artifacts with no statistically significant differences among the observers. However, higher kappa values were achieved with titanium implants for all observers and scan modes.

Although no information on the operation of the MAR algorithm and AINO filter is available, the Planmeca AINO uses adaptive noise algorithms or adaptive image de-noising techniques. These techniques are either semiautomatically or automatically adaptive and offer better smooth subsurface recovery contained in the true image. One explanation for the more accurate detection of the artificially created dehiscences with the use of the MAR module and the AINO filter is the consideration of both spatial information and intensity information between the dehiscences and the implant itself. MAR uses a selected threshold, and all voxels with higher density are corrected. When using both MAR and AINO together, the variables on signal information can be used to predict the pixel values. Minimizing the total variation of the signal removes unwanted details while preserving such details as edges and the relationship between dehiscences and implants.

The limitations of this investigation are the use of only 1 CBCT unit, variations in observer experience, simulated dehiscence defects, small sample number, use of an in vitro model without motion artifacts, and the same exposure parameters for all scans. It would be useful to perform this study with different CBCT units using various kVp, mA, and FOV settings and a larger sample size.

CONCLUSIONS

Despite the limitations of this study, both the MAR algorithm and the AINO filter enhanced the efficacy of the detection of artificially created dehiscences in proximity to implants. The combined use of these techniques is recommended for detecting peri-implant dehiscences. The detection of dehiscences was more accurate with titanium implants. There were no significant differences in agreement among and between the observers, but weighted kappa coefficients were lowest in the scan mode without MAR/without AINO than in the other 3 modes.

REFERENCES

1. Blanco J, Alonso A, Sanz M. Long-term results and survival rate of implants treated with guided bone regeneration: a 5-year case series prospective study. *Clin Oral Implants Res*. 2005;16:294-301.
2. Xu X, Xu L, Jiang J, Wu J, Li X, Jing W. Accuracy analysis of alveolar dehiscence and fenestration of maxillary anterior teeth of Angle class III by cone-beam CT. *Beijing Da Xue Xue Bao Yi Xue Ban*. 2018;50:104-109. [in Chinese].
3. Leung CC, Palomo L, Griffith R, Hans MG. Accuracy and reliability of cone-beam computed tomography for measuring alveolar bone height and detecting bony dehiscences and fenestrations. *Am J Orthod Dentofacial Orthop*. 2010;137:S109-S119.
4. Mengel R, Kruse B, Flores-de-Jacoby L. Digital volume tomography in the diagnosis of peri-implant defects: an in vitro study on native pig mandibles. *J Periodontol*. 2006;77:1234-1241.
5. Noujeim M, Prihoda T, Langlais R, Nummikoski P. Evaluation of high-resolution cone beam computed tomography in the detection of simulated interradicular bone lesions. *Dentomaxillofac Radiol*. 2009;38:156-162.
6. Angelopoulos C, Aghaloo T. Imaging technology in implant diagnosis. *Dent Clin North Am*. 2011;55:141-158.
7. Bechara B, McMahan CA, Nasseh I, et al. Number of basis images effect on detection of root fractures in endodontically treated teeth using a cone beam computed tomography machine: an in vitro study. *Oral Surg Oral Med Oral Pathol Oral Radiol*. 2013;115:676-681.
8. Scarfe WC, Farman AG, Sukovic P. Clinical applications of cone-beam computed tomography in dental practice. *J Can Dent Assoc*. 2006;72:75-80.
9. Kolsuz ME, Bagis N, Orhan K, Avsever H, Demiralp KO. Comparison of the influence of FOV sizes and different voxel resolutions for the assessment of periodontal defects. *Dentomaxillofac Radiol*. 2015;44:20150070.
10. Schulze R, Heil U, Gross D, et al. Artefacts in CBCT: a review. *Dentomaxillofac Radiol*. 2011;40:265-273.
11. Ren L, Yin FF, Chetty IJ, Jaffray DA, Jin JY. Feasibility study of a synchronized-moving-grid (SMOG) system to improve image quality in cone-beam computed tomography (CBCT). *Med Phys*. 2012;39:5099-5110.
12. Parrone MT, Bechara B, Deahl S.T. 2nd, Ruparel NB, Katkar R, Noujeim M. Cone beam computed tomography image optimization to detect root fractures in endodontically treated teeth: an in vitro (phantom) study. *Oral Surg Oral Med Oral Pathol Oral Radiol*. 2017;123:613-620.
13. Kocasarac Demirturk H, Ustaoglu G, et al. Evaluation of artifacts generated by titanium, zirconium, and titanium−zirconium alloy dental implants on MRI, CT, and CBCT images: a phantom study. *Oral Surg Oral Med Oral Pathol Oral Radiol*. 2019;127:535-544.

14. Bland JM, Altman DG. Measuring agreement in method comparison studies. *Stat Methods Med Res*. 1999;8:135-160.
15. Kamburoglu K, Kolsuz E, Murat S, Eren H, Yuksel S, Paksoy CS. Assessment of buccal marginal alveolar peri-implant and periodontal defects using a cone beam CT system with and without the application of metal artefact reduction mode. *Dentomaxillofac Radiol*. 2013;42:20130176.
16. de-Azevedo-Vaz SL, Vasconcelos Kde F, Neves FS, Melo SL, Campos PS, Haiter-Neto F. Detection of periimplant fenestration and dehiscence with the use of two scan modes and the smallest voxel sizes of a cone-beam computed tomography device. *Oral Surg Oral Med Oral Pathol Oral Radiol*. 2013;115:121-127.
17. Baltacioglu IH, Orhan K. Comparison of diagnostic methods for early interproximal caries detection with near-infrared light transillumination: an in vivo study. *BMC Oral Health*. 2017;17:130.
18. Nikneshan S, Valizadeh S, Javanmard A, Alibakhshi L. Effect of voxel size on detection of external root resorption defects using cone beam computed tomography. *Iran J Radiol*. 2016;13:e34985.
19. Yamamoto-Silva FP, de Oliveira Siqueira CF, Silva M, et al. Influence of voxel size on cone-beam computed tomography-based detection of vertical root fractures in the presence of intracanal metallic posts. *Imaging Sci Dent*. 2018;48:177-184.
20. Baltacioglu IH, Eren H, Yavuz Y, Kamburoglu K. Diagnostic accuracy of different display types in detection of recurrent caries under restorations by using CBCT. *Dentomaxillofac Radiol*. 2016;45:20160099.
21. Bagis N, Eren H, Kolsuz ME, Kurt MH, Avsever H, Orhan K. Comparison of the burr and chemically induced periodontal defects using different field-of-view sizes and voxel resolutions. *Oral Surg Oral Med Oral Pathol Oral Radiol*. 2018;125:260-267.
22. de-Azevedo-Vaz SL, Peyneau PD, Ramirez-Sotelo LR, de Faria Vasconcelos K, Campos PSF, Haiter-Neto F. Efficacy of a cone beam computed tomography metal artifact reduction algorithm for the detection of peri-implant fenestrations and dehiscences. *Oral Surg Oral Med Oral Pathol Oral Radiol*. 2016;121:550-556.
23. Queiroz PM, Santaella GM, Da Paz TD, Freitas DQ. Evaluation of a metal artefact reduction tool on different positions of a metal object in the FOV. *Dentomaxillofac Radiol*. 2017;46:20160366.
24. Bechara B, McMahan CA, Geha H, Noujeim M. Evaluation of a cone beam CT artefact reduction algorithm. *Dentomaxillofac Radiol*. 2012;41:422-428.
25. Bechara B, Alex McMahan C, Moore WS, Noujeim M, Teixeira FB, Geha H. Cone beam CT scans with and without artefact reduction in root fracture detection of endodontically treated teeth. *Dentomaxillofac Radiol*. 2013;42:20120245.
26. Kamburoğlu K, Yilmaz F, Yeta EN, Ozen D. Assessment of furcal perforations in the vicinity of different root canal sealers using a cone beam computed tomography system with and without the application of artifact reduction mode: an ex vivo investigation on extracted human teeth. *Oral Surg Oral Med Oral Pathol Oral Radiol*. 2016;121:657-665.
27. Vasconcelos TV, Bechara BB, McMahan CA, Freitas DQ, Noujeim M. Evaluation of artifacts generated by zirconium implants in cone-beam computed tomography images. *Oral Surg Oral Med Oral Pathol Oral Radiol*. 2017;123:265-272.

Reprint requests:

Seval Bayrak
Faculty of Dentistry
Bolu Abant Izzet Baysal University
14000, Golkoy
Bolu
Turkey
dtseval@hotmail.com